Monthly Notices of the ROYAL ASTRONOMICAL SOCIETY

MNRAS **472,** 542–549 (2017) doi:10.1093/mnras/stx1986
Advance Access publication 2017 August 4

General relativistic numerical simulation of sub-Keplerian transonic accretion flows on to black holes: Schwarzschild space–time

Jinho Kim,[1⋆] Sudip K. Garain,[1⋆] Dinshaw S. Balsara[1] and Sandip K. Chakrabarti[2,3]

[1]*Department of Physics, University of Notre Dame, Notre Dame, IN 46556, USA*
[2]*S. N. Bose National Center for Basic Sciences, Block JD, Sector III, Salt Lake, Kolkata 700098, India*
[3]*Indian Center for Space Physics, 43 Chalantika, Garia St Rd., Kolkata 700084, India*

Accepted 2017 August 1. Received 2017 July 31; in original form 2017 March 16

ABSTRACT

We study time evolution of sub-Keplerian transonic accretion flows on to black holes using a general relativistic numerical simulation code. We perform simulations in Schwarzschild space–time. We first compare one-dimensional simulation results with theoretical results and validate the performance of our code. Next, we present results of axisymmetric, two-dimensional simulation of advective flows. We find that even in this case, for which no complete theoretical analysis is present in the literature, steady-state shock formation is possible.

Key words: accretion, accretion discs – black hole physics – hydrodynamics – shock waves – methods: numerical.

1 INTRODUCTION

Independent of the source of matter supply, an accretion flow around a black hole is necessarily transonic, i.e. it must pass through one or more sonic point(s). An accretion flow on a gravitating star, whose specific angular momentum is everywhere or almost everywhere lower than that of the local Keplerian value may be termed as a sub-Keplerian flow. Theoretical calculations as well as numerical simulations of sub-Keplerian transonic accretion flows around black holes have shown that such flows can have standing shocks for appropriate choice of the flow parameters such as the specific energy ϵ and specific angular momentum l of the accreting material (Chakrabarti 1989, 1990a, hereafter C89, C90, respectively). Paradoxical as it may sound, the flow decides to slow down just a few to few tens of gravitational radii away from the horizon, simply because the centrifugal barrier becomes very strong as compared to the gravity. However, the barrier is not unsurmountable and flow simply passes through a shock transition to satisfy boundary conditions, as is normal in many astrophysical circumstances. The shock can be simply standing or propagating away depending on the flow parameters and the dissipative and cooling processes present in the flow (C89, C90; Chakrabarti 1996c, and references therein). Using numerical simulations with smoothed particle hydrodynamics, these shocks have been shown to be stable in both one- and two-dimensional simulations (Chakrabarti & Molteni 1993; Molteni, Lanzafame & Chakrabarti 1994, hereafter CM93, MLC94, respectively). They were found to propagate away for high enough viscosity (Chakrabarti & Molteni 1995). The post-shock region, which is known as CENtrifugal pressure supported BOundary Layer (or CENBOL), as in any other astrophysical flows, is found to be extremely useful to explain detailed spectral properties of the black hole accretion disc quite satisfactorily (Chakrabarti & Titarchuk 1995; Chakrabarti 1997, hereafter CT95, C97, respectively). The so-called two-component advective flow (TCAF) model, proposed in CT95 and C97, describes the most general structure of an accretion disc which consists of two transonic components, namely, an optically thick (optical depth, $\tau \gg 1$), geometrically thin Keplerian disc and an optically thin ($\tau < 1$), geometrically thick sub-Keplerian flow. Shock is formed in the sub-Keplerian component which has higher radial infalling velocity than the other component. In the post-shock region, i.e. inside the CENBOL, these two components mix up due to turbulence and heat (CT95) and form an optically slim ($\tau \sim 1$), geometrically thick disc and continues its journey towards the central object. The CENBOL itself becomes responsible for the non-thermal power-law component of the observed spectrum.

Recently, TCAF model has been included in HEASARC's spectral analysis software package XSPEC (Arnaud 1996) and is being used to study the spectral as well as timing properties of several black hole candidates (Debnath, Chakrabarti & Mondal 2014; Mondal, Debnath & Chakrabarti 2014; Chakrabarti, Mondal & Debnath 2015; Debnath, Mondal & Chakrabarti 2015a; Debnath et al. 2015b; Chatterjee et al. 2016; Jana et al. 2016). It has been demonstrated that this model explains the observed data very well. In outbursting sources, the shocks were found to be propagating as well – steadily moving towards the black hole in the rising phase and moving away from it in the declining phase. Simulations of

⋆ E-mail: jkim46@nd.edu (JK); sgarain@nd.edu (SKG)

inviscid accretion flow with presence of a power-law cooling show that shock can oscillate about a certain mean location, particularly when there is resonance between the cooling and the infall time-scales. This may be considered to be an explanation of the origin of low-frequency quasi-periodic oscillations (LFQPOs; Molteni, Sponholz & Chakrabarti 1996a; Chakrabarti, Acharyya & Molteni 2004). Such oscillations have been shown to be present and stable when real Compton cooling is present in the flow as well (Garain, Ghosh & Chakrabarti 2012, 2014, hereafter, GGC12, GGC14, respectively). These intriguing properties of the CENBOL clearly demand conducting robust numerical experiments, which we set out to do in a series of papers.

Several numerical experiments are already present in the literature which study shock structures in the sub-Keplerian flow around black holes. For one- and two-dimensional inviscid, adiabatic flows, it has been shown that a sub-Keplerian axisymmetric flow with and without shock is stable (CM93, MLC94; Molteni, Ryu & Chakrabarti 1996b, hereafter MRC96). New codes have been tested against such non-linear solutions as well (Toth, Keppens & Botchev 1998). Numerical simulations of adiabatic viscous flow also demonstrate the stability of these standing shock waves (Giri & Chakrabarti 2012; Lee et al. 2016). More recently, two-dimensional axisymmetric numerical simulations of viscous flow in presence of power-law and Compton cooling show that an advective flow actually splits into two components when appropriate viscosity parameters and cooling processes are chosen (Giri & Chakrabarti 2013; Giri, Garain & Chakrabarti 2015, hereafter, GC13, GGC15, respectively). As the sub-Keplerian flow advects towards the central black hole, angular momentum transport and condensation due to cooling on the equatorial plane help the flow to segregate into two distinct advective components, each being separately transonic. The component near the equatorial plane has been shown to have the properties very similar to a standard Keplerian disc (Shakura & Sunyaev 1973). This component is surrounded by the sub-Keplerian component which will have the steady shock. Thus, these results show that a stable TCAF formation is indeed possible.

In case of magnetized accretion disc, magnetorotational instability (MRI; Balbus & Hawley 1991; Hawley & Balbus 1992) can make the disc turbulent and this turbulence may transport angular momentum outwards efficiently. However, it has been shown that turbulence triggered by MRI produces the value of the alpha viscosity parameter $\sim$0.01 (Brandenburg et al. 1995; Hawley, Gammie & Balbus 1995, 1996; Smak 1999; Arlt & Rüdiger 2001; King, Pringle & Livio 2007; Kotko & Lasota 2012). In the literature, many authors from various groups published results of analytical viscous solutions as well as viscous hydrodynamic simulations where it has been shown that the shock is stable if the viscosity parameter is lower than a critical viscosity parameter (Chakrabarti 1990b,1996a; Chakrabarti & Molteni 1995; Lanzafame, Molteni & Chakrabarti 1998; Lanzafame et al. 2008; Lee, Ryu & Chattopadhyay 2011; Das et al. 2014; Lee et al. 2016). Also, there have been many stability studies of shock (Nakayama 1992, 1994; Nobuta & Hanawa 1994; Gu & Foglizzo 2003; Gu & Lu 2006), but it was shown that even under non-axisymmetric perturbations, the shock tends to persist, albeit, as a deformed shock (Molteni, Tóth & Kuznetsov 1999).

Despite all these important developments, almost all the above-mentioned simulations have been performed using the so-called pseudo-Newtonian potential (Paczyński & Wiita 1980) which mimics the Schwarzschild space–time. This potential retains the particle properties of the Schwarzschild geometry in the sense that the marginally bound and marginally stable orbits are located at exactly the same places as in general relativistic (GR) calculation. However, several properties in the strong gravity limit just outside of the horizon are not retained with precision. For instance, the energy released at the marginally stable orbit or the velocity of matter on the horizon is different. Thus, though the results were satisfactory, it was difficult to judge if any of the effects observed were artefacts of the potential. Fortunately, even in GR framework, in Kerr space–time, such shocks have been shown to exist (C90; Chakrabarti 1996b, hereafter C96b). And it became clearer that the shocks in black hole accretion are indeed possible only because of the presence of the inner sonic point between the marginally bound and marginally stable orbits where strong gravity is important. Strong gravity forces the flow to have an inner sonic point. Most importantly in accretion flow configurations, the solution passing through the inner sonic point has higher entropy than that passing through the outer sonic point. So the flow generates entropy at the shock and then passes through the inner sonic point. The location of the sonic point is the closest indicator of a stable fluid (unlike the marginally stable orbit, which is the closest indicator for a particle trajectory). Thus, there are all the more reasons to verify these results using a full relativistic framework. In this work, we perform a GR simulation of the sub-Keplerian flow in Schwarzschild space–time. To our knowledge, no numerical experiment has so far been performed which tests the possibility of a stable CENBOL formation in general relativity.

This paper is organized as follows. In Section 2, we present the analytical method to calculate the one-dimensional flow properties in Schwarzschild space–time. In Section 3, we present the GR equations which are solved numerically and the numerical procedure we use for doing this. In the next section, we present the results for one- and two-dimensional simulations. Finally, we present our conclusions.

In this paper, we choose $R_g = GM_{\rm BH}/c^2$ as the unit of distance, $R_g c$ as the unit of angular momentum and R_g/c as the unit of time. In addition, we choose the geometric units $G = M_{\rm BH} = c = 1$ (G is gravitational constant, $M_{\rm BH}$ is the mass of the black hole and c is the unit of light). Thus, $R_g = 1$, and angular momentum and time are measured in dimensionless units.

2 ANALYTICAL SOLUTION

The GR study of transonic flows has been done extensively by Chakrabarti (C90, C96b). Therefore, we do not describe all the details here. However, for completeness, we mention only the important equations for Schwarzschild space–time.

For this calculation, we use Boyer–Lindquist coordinates (t, r, θ, ϕ). The line element in Schwarzschild space–time is given as follows:

$$\begin{aligned} {\rm d}s^2 &= g_{\mu\nu}{\rm d}x^\mu {\rm d}x^\nu \\ &= -\left(1-\frac{2}{r}\right){\rm d}t^2 + \left(1-\frac{2}{r}\right)^{-1}{\rm d}r^2 + r^2{\rm d}\theta^2 + r^2\sin^2\theta{\rm d}\phi^2. \end{aligned} \tag{1}$$

We are interested in the flow close to the equatorial plane, so $\theta = \pi/2$ is assumed for analytical study.

In absence of viscosity and any heating or cooling, one can find the conserved specific energy as (C96b)

$$\epsilon = hu_t = \frac{1}{1-na^2}u_t, \tag{2}$$

where, $n = 1/(\Gamma - 1)$ is the polytropic index, Γ being the adiabatic index and $h = 1/(1 - na^2)$ is the enthalpy, a being the sound speed. Also,

$$u_t = \left[\frac{1 - \frac{2}{r}}{(1 - V^2)(1 - \Omega l)}\right]^{1/2}. \tag{3}$$

Here,

$$\Omega = \frac{u^\phi}{u^t} = -\frac{l g_{tt}}{g_{\phi\phi}} = \frac{l}{r^2}\left(1 - \frac{2}{r}\right), \tag{4}$$

and $l = -u_\phi/u_t$ is the specific angular momentum. Also,

$$V = \frac{v}{(1 - \Omega l)^{1/2}}, \tag{5}$$

where

$$v = \left(-\frac{u_r u^r}{u_t u^t}\right)^{1/2}. \tag{6}$$

The entropy accretion rate (C89, C96b) is given by

$$\dot{\mu} = \left(\frac{a^2}{1 - na^2}\right)^n V\,(1 - \Omega l)^{1/2}\, u_t r^2. \tag{7}$$

We follow the usual solution procedures use in transonic flows (C89, C90) to calculate $V(r)$ and radial dependence of other required quantities. By differentiating equations (2) and (7) with respect to r and eliminating terms involving $\mathrm{d}a/\mathrm{d}r$, we find following expression as the gradient of $V(r)$:

$$\frac{\mathrm{d}V}{\mathrm{d}r} = \frac{V\left(1 - V^2\right)\left[1 - 2ra^2 + 3a^2 - \frac{\Omega l}{1 - \Omega l}(r - 3)\right]}{r\,(r - 2)\left(a^2 - V^2\right)}. \tag{8}$$

We can readily see that for $l = 0$, we recover the similar expression for Bondi flow on to a black hole (equation 1.29 of C90). At the sonic point, both numerator and the denominator vanish and one obtains the so-called sonic point condition as

$$V_c = a_c,$$

and

$$a_c^2 = \frac{1}{2r_c - 3}\left[1 - \frac{\Omega l}{1 - \Omega l}(r_c - 3)\right], \tag{9}$$

where, r_c, is called the sonic radius.

To find a complete solution from the horizon to infinity, one needs to supply the specific energy ϵ and the specific angular momentum l. If the supplied parameters allow the accretion solution to have a shock in the sense that Rankine Huguniot conditions are satisfied, then the shock location can be found by determining a constant, C, which remains invariant across the shock (C89, C90). It is found that this invariant quantity is the same in Schwarzschild space–time and in pseudo-Newtonian potential (C90), as this is a local equation. Therefore, we use the following expression,

$$C = \frac{[\Gamma M + (1/M)]^2}{2 + (\Gamma - 1)M^2} \tag{10}$$

to determine the shock location for this calculation (Chakrabarti & Das 2001). Here, we use $M = V/a$ as the definition of Mach number.

3 NUMERICAL SIMULATION PROCEDURE

We use so-called Valencia formulation to numerically solve the relativistic hydrodynamic equation (Banyuls et al. 1997). This formulation gives flux conservative form of the system of hydrodynamics equation in the framework of 3 + 1 formalism. It has been applied very successfully in computational fluid dynamics. In our coordinate system, the conservative variables (q) and primitive variables (w) are

$$q = \begin{pmatrix} D \\ S_r \\ S_\theta \\ S_\phi \\ \tau \end{pmatrix} \equiv \begin{pmatrix} \rho W \\ \rho h W^2 v_r \\ \rho h W^2 v_\theta \\ \rho h W^2 v_\phi \\ \rho h W^2 - P - D \end{pmatrix}, \quad w = \begin{pmatrix} \rho \\ v^r \\ v^\theta \\ v^\phi \\ P \end{pmatrix}. \tag{11}$$

Here, ρ is the fluid rest mass density, P is the pressure and h is the specific enthalpy. They are measured in the comoving frame of the fluid. v^i is the fluid velocity measured by Eulerian observer. W is the Lorentz factor and defined as $W = 1/\sqrt{1 - \gamma_{ij} v^i v^j}$. Here, γ_{ij} are the spatial part of the metric components $g_{\mu\nu}$. The radial and angular velocity in the Eulerian frame can be expressed in terms of v in equation (6) and Ω in equation (4):

$$v^r = \frac{u^r}{W} = \left(1 - \frac{2}{r}\right)^{\frac{1}{2}} v \tag{12}$$

$$v^\phi = \frac{u^\phi}{W} = \left(1 - \frac{2}{r}\right)^{-\frac{1}{2}} \Omega. \tag{12}$$

Assuming axisymmetry ($\frac{\partial}{\partial\phi} = 0$), the hydrodynamical equations in the curved space–time which is described in equation (1) can be written as follows:

$$\frac{\partial\left(\sqrt{\gamma} q\right)}{\partial t} + \frac{\partial\left(\sqrt{-g} f^r\right)}{\partial r} + \frac{\partial\left(\sqrt{-g} f^\theta\right)}{\partial\theta} = \sqrt{-g}\,\Sigma, \tag{13}$$

where

$$f^r = \begin{bmatrix} D v^r \\ S_r v^r + P \\ S_\theta v^r \\ S_\phi v^r \\ \tau v^r + P v^r \end{bmatrix},$$

$$f^\theta = \begin{bmatrix} D v^\theta \\ S_r v^\theta \\ S_\theta v^\theta + P \\ S_\phi v^\theta \\ \tau v^\theta + P v^\theta \end{bmatrix},$$

$$\Sigma = \begin{bmatrix} 0 \\ -\frac{\rho h W^2}{r}\left(\frac{1}{r-2}(1 + v_r v^r) - v_\theta v^\theta - v_\phi v^\phi\right) + \frac{2P}{r} \\ \cot\theta\left(\rho h W^2 v_\phi v^\phi + P\right) \\ 0 \\ -\frac{\rho h W^2 v^r}{r(r-2)} \end{bmatrix}. \tag{14}$$

Here, $\sqrt{\gamma}$ and $\sqrt{-g}$ are the determinants of spatial and space–time metric, respectively. From the Schwarzschild metric shown in equation (1), we have $\sqrt{\gamma} = r^2 \sin\theta\,(1 - 2/r)^{-1/2}$, and $\sqrt{-g} = r^2 \sin\theta$. For the spherically symmetric cases, $\frac{\partial}{\partial\theta} = 0$. Equation (14) consists of the continuity, three momentum and energy equations. We clearly see the conservation of total rest mass (baryon number) and angular momentum in the first and fourth rows of

equation (14). Particularly, the terms of Σ in the momentum equation contain the gravitational and the centrifugal forces. The gravitational force which is purely radial in the Schwarzschild metric is shown in the first term of the second row of Σ. The second and third terms in the second row as well as the first term in the third row represent the centrifugal force by the rotation velocity. Since the centrifugal force, exerted by the v^{ϕ}, is not purely radial, it contributes to both $r-$ and $\theta-$ momentum equations. (cf. the centrifugal force exerted by the v^{θ} is purely radial. Therefore, it appears only in the radial momentum equation.) Note that the last terms in the Σ of the momentum equations are the additional terms in the spherical polar coordinates system. The fifth row of Σ is the sink or source of the energy contributed by gravity.

We use the ideal gas equation of state which can be written in the following form:

$$P = (\Gamma - 1)\,\rho e, \tag{15}$$

where e is the specific internal energy. The above equation of state provides the expression of specific enthalpy:

$$h = 1 + \frac{\Gamma}{\Gamma - 1}\frac{P}{\rho}. \tag{16}$$

In this paper, we solve the above hydrodynamic equations using a numerical code developed by Kim et al. (2012). The details of the code can be found in Kim et al. (2012). The most useful property of this code is that it can be applied to any space–time metric in any coordinate system. This code uses finite volume methods to ensure local conservation of the fluid in the computational grid. Therefore, the code can guarantee total mass and angular momentum conservations which appear in the first and fourth rows of equation (14). For the treatment of the discontinuous behaviours of the fluid such as shocks, rarefactions or contact discontinuities, the high-resolution shock-capturing techniques are applied in the code. We use the third-order slope limiter proposed by Shibata (2003) which is based on the *minmod* function. For the flux approximation, we use the HLL method (Harten, Lax Peter & van Leer 1983). The HLL method has some dissipation but the results are very stable. For the time integration, we use the third-order three-stage strong stability-preserving Runge–Kutta method which is known as Shu–Osher method (Shu & Osher 1988).

4 RESULTS

We use inflow boundary condition at the outer boundary located at $r_{\rm out} = 100$. The inner boundary is placed at $r_{\rm in} = 2.1$ and we use the extrapolated values of the primitive variables for the inner ghost cells. These inner ghost cells are located outside of the event horizon. In this paper, we present results of one-dimensional and two-dimensional simulations. For better resolution close to the central black hole, we logarithmically binned the radial direction in 300 zones for all the simulation results presented here. For two-dimensional simulations, in addition to above-mentioned radial binning, we used 100 equi-spaced zones in polar direction. The innermost radial zone (Δr) has a size of 2.72×10^{-2} and the outermost zone has a size of 1.28.

For these simulations, we need values of the primitive variables (see equation 11) at $r = r_{\rm out}$. For all the simulations, we set $v^{\theta} = 0$. The density of the incoming matter at $r_{\rm out}$ is normalized to 1. In the absence of self-gravity and heating or cooling, the density is scaled out and the simulation results remain valid for any accretion rate (MRC96; Giri at al. 2010, hereafter GCSR10). We evaluate $V(r = r_{\rm out})$ by solving equation (8) for a given pair of conserved flow variables. Subsequently, the sound speed $a_{\rm out} = a(r = r_{\rm out})$ is evaluated using equation (2). Next, using equations (5), (6) and (12), we evaluate $v^{r}(r = r_{\rm out})$ and $v^{\phi}(r = r_{\rm out})$. Pressure of the incoming matter is evaluated from the sound speed $a_{\rm out}$ using equation (16). These values are maintained in the ghost zones of the outer boundary of our computational domain. As an initial condition, we put floor values for the density to be $\rho_{\rm floor} = 10^{-10}$ (in normalized unit) and the corresponding floor value of pressure inside the computational domain. Floor value of the pressure is chosen such that the sound speed (or temperature) of the background matter is same as that of incoming matter (MRC96, GC13). Thus, once we know $a_{\rm out}$, we evaluate the value of the pressure floor using equation (16) by substituting $\rho = 10^{-10}$ in this equation. Then, the value of pressure floor is $P_{\rm floor} = na_{\rm out}^2\rho_{\rm floor}/[(1 - na_{\rm out}^2)(n + 1)]$. Initially, the velocity components in the floor grids are set to zero. Thus, initially, as the matter rushes towards the black hole, it fills the vacuum rapidly. After the matter reaches the inner boundary, the flow starts to feel the pressure and centrifugal force.

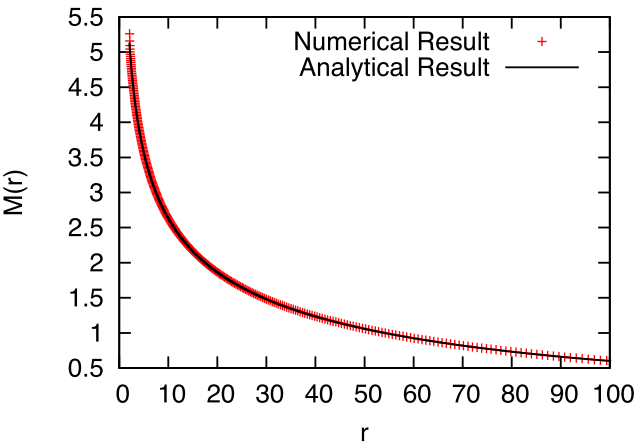

Figure 1. Comparison of radial Mach number variation for Bondi accretion flow. Black solid line is obtained using analytical method, whereas red plus signs are the simulation results after steady state is reached. They appear to be indistinguishable.

4.1 One-dimensional, spherically symmetric Bondi accretion

For a given ϵ, the analytical structure of a spherically symmetric Bondi accretion flow is completely determined ($l = 0$ for this flow). For the comparative study, we choose $\epsilon = 1.015$. This choice gives $V = 0.053$ and $a = 0.088$ at $r_{\rm out}$, and the sonic point at $r = 54.04$. Note that, just the energy was sufficient to determine all the quantities as the other conditions come from transonicity (equation 9, C90). In Fig. 1, we compare the radial variations of Mach number, defined as $M(r) = V(r)/a(r)$. The black solid line represents the analytical result, whereas the red plus signs represent the numerical simulation result. Clearly, they are indistinguishable. Dynamical time, $t_{\rm dyn}$ (defined as the time required for matter to reach inner boundary from $r_{\rm out}$ in steady state), is found to be $t_{\rm dyn} \sim 991$ for this simulation and we ran the simulation for more than $20t_{\rm dyn}$ ($t \sim 19\,800$). Also, we ran some more cases by varying the number of radial zones ranging from 150 to 600 and verified that the results remained converged. Note that the inner boundary places at $r_{\rm in} = 2.5$ for the lower resolution case in order to prevent the inner ghost cells from locating inside the event horizon.

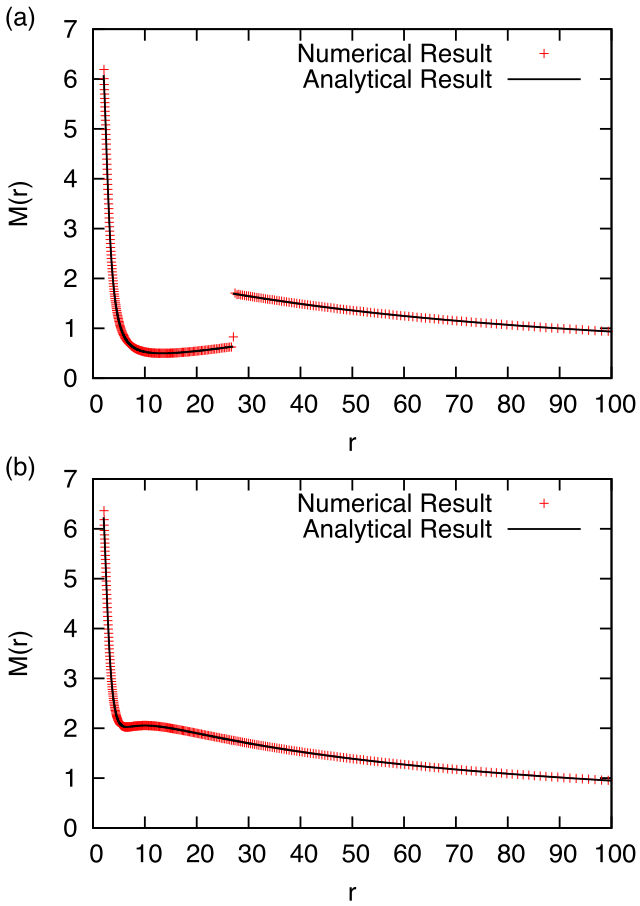

Figure 2. Comparison of radial Mach number variation for one-dimensional axisymmetric accretion flows. (a) represents results where shock is present and (b) represents results where no shock formed and the flow is supposed to pass only through the outer sonic point. Black solid line is obtained using analytical method, whereas red plus signs are the simulation results.

4.2 One-dimensional accretion flow with non-zero angular momentum

When angular momentum is present, the flow structure changes significantly depending on its strength. As discussed earlier, depending on the values of ϵ and l, the accretion flow may or may not have any shock. In this section, we present the results of two simulations in one dimension. One solution has a shock and the other does not. As discussed in C89 (see Fig. 3); C90 (see Chaps 3 and 6), the accretion solution having a shock first passes through the outer sonic point, makes a transition to the sub-sonic branch at the shock and then passes through the inner sonic point just before being supersonically accreted by the black hole. On the other hand, when ϵ and l are such that it is not possible to have a shock, the flow passes only through the outer or inner sonic point before disappearing behind the horizon. However, such a flow still can slow down as it approaches the black hole because of the centrifugal force. In Fig. 2(a), we present the radial variation of Mach number, $M(r)$, at the final steady state for the accretion flow which has a shock. As before, the black solid line represents the analytical result and the red plus signs represent the simulation result. $\epsilon = 1.007$ and $l = 3.4$ are chosen for this simulation. Analytical calculation gives $V = 0.0645$ and $a = 0.0691$ at $r = 100$. The outer sonic point, shock and inner sonic point are located at $r = 89.59$, 26.98 and 5.38, respectively. As can be seen, our 1D simulation has captured all the locations properly. For this case, dynamical time is found to be 1150 and the simulation was run till $20t_{\rm dyn}$ ($t \sim 23\,000$). We have also computed ϵ and l from the simulation result and verified that these two quantities remain constant along the flow.

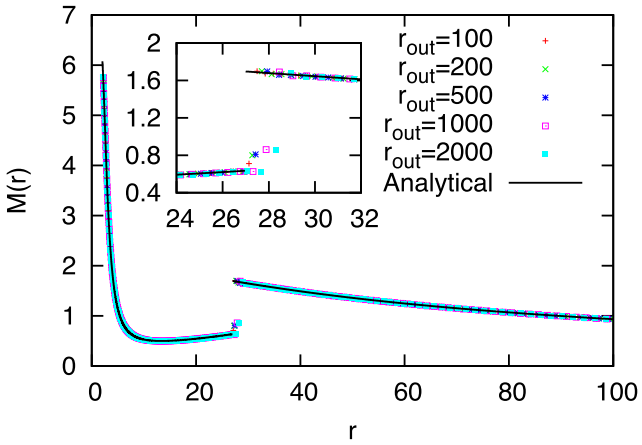

Figure 3. Results of rerun for the case presented in Fig. 2(a) by moving $r_{\rm out}$ to 200, 500, 1000 and 2000. Green, blue, magenta and cyan (cross, star, open square and filled square) points represent the simulation results for $r_{\rm out} = 200, 500, 1000$ and 2000, respectively. We can clearly see that the shock locations do not get affected if we change $r_{\rm out}$. In the inset, we show the zoomed in part around the shock location.

Fig. 2(b) shows the radial variation of M for a case where there is no shock in the accretion solution and is expected to pass only through the outer sonic point. We choose $\epsilon = 1.007$ and $l = 3.25$ to compute the outer boundary values for this simulation. For this case, dynamical time is found to be 920 and the simulation was run till $20t_{\rm dyn}$ ($t \sim 18\,400$). The outer sonic point is located at $r = 91.92$ for these parameters. As can be seen from the figure, analytical and numerical results are nearly inseparable and hence, we see that numerical simulation has captured this location very well. We may mention in passing that the simulations presented in the literature are primarily for supersonic injection to save computational time. However, our efficient method allows us to inject the flow at sub-sonic Mach number.

In order to verify that the shock location is not affected by the outer boundary, we rerun the case presented in Fig. 2(a) by moving $r_{\rm out}$ to 200, 500, 1000 and 2000. All these simulations have been run using 300 zones in the radial direction. In Fig. 3, we present these simulation results. Green, blue, magenta and cyan (cross, star, open square and filled square) points represent the simulation results for $r_{\rm out} = 200, 500, 1000$ and 2000, respectively. In the inset, we show the zoomed in part around the shock location. Comparison of shock location for various $r_{\rm out}$ shows that it does not get affected if we change $r_{\rm out}$. Slight mismatch for $r_{\rm out} = 1000$ and 2000 may be due to the grid size variation at the shock location.

4.3 Two-dimensional simulations

Realistically, an accretion disc is three dimensional. However, assuming axisymmetry, we can study the disc structure in two dimensions. On the other hand, the theoretical formalism of transonic flows (Chakrabarti 1996b) is developed for flows in vertical equilibrium which is quite thin. Indeed, the shock location and Mach number variation depend on the model assumption. Most interestingly, it was shown (GCSR10) that the pre-shock flow behaves as

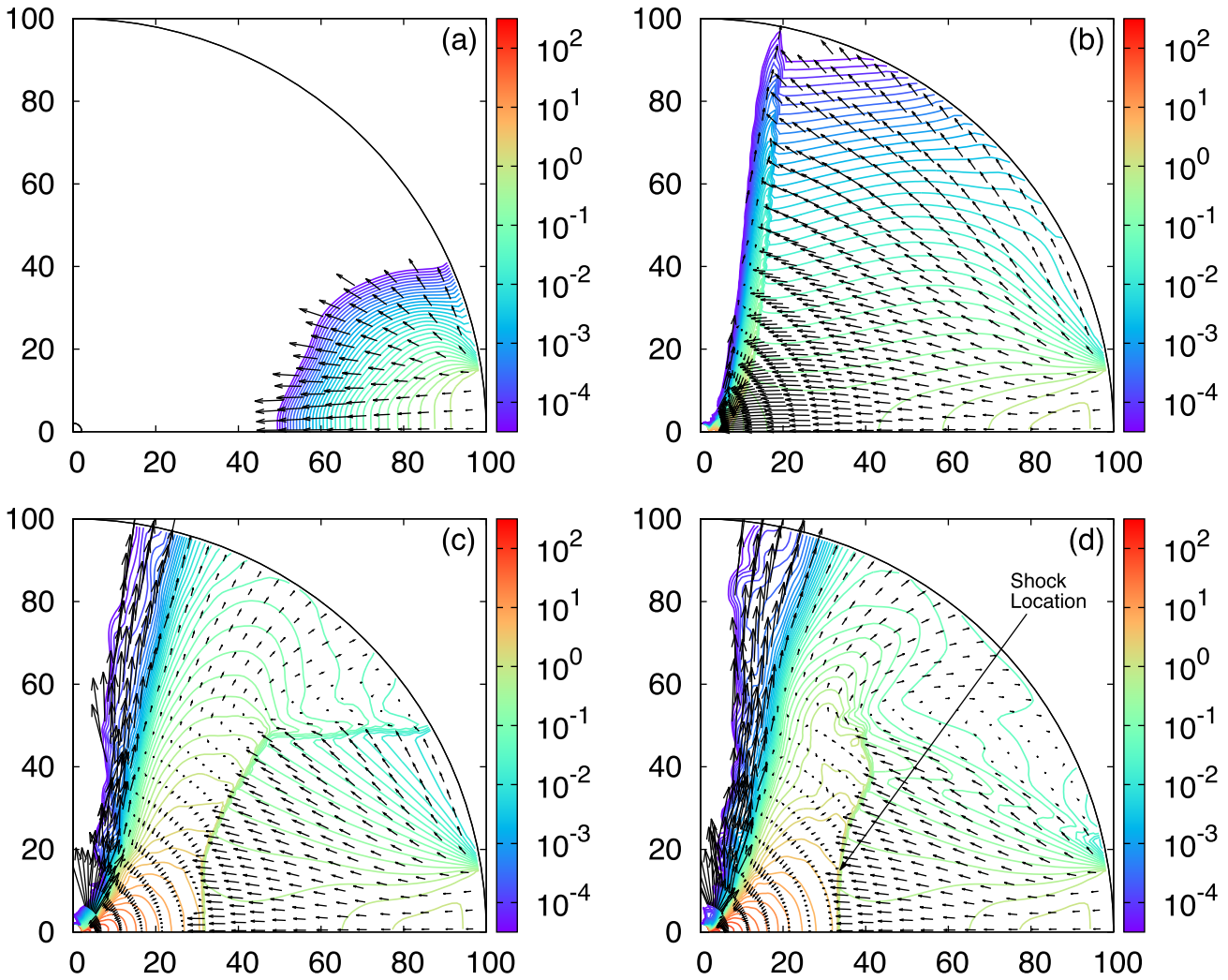

Figure 4. Contours of normalized density, overplotted with velocity vectors at four different time. Snapshots (a), (b), (c) and (d) are plotted at times 158, 496, 2250 and 30 000, respectively. The corresponding dynamical times are 0.11, 0.33, 1.5 and 20, respectively. See text for details.

a conical flow, while the post-shock behaves as a flow in vertical equilibrium. So, a direct comparison with theoretical result is not possible in a two-dimensional simulation. On the other hand, in Section 4.2, we showed that our simulation result matches with the theory very well. Thus, the results obtained in two dimensions may be trusted.

For the results presented here, we do the simulation in (r, θ) coordinates. Simulation domain extends from $r_{\rm in} = 2.1$ to $r_{\rm out} = 100$ in radial direction and $[0 : \pi/2]$ in polar direction. The incoming matter enters the simulation box at $r_{\rm out}$ through one-tenth of polar zones starting from equatorial plane (GCSR10, GGC12, GGC14). For this simulation, we evaluate the outer boundary values using vertical equilibrium model. We choose $\epsilon = 1.0022$ and $l = 3.36$, and this choice gives $V = 0.0825$ and $a = 0.0526$ at $r_{\rm out}$. For these parameters, the one-dimensional analytical calculation predicts the shock to be located at 15.77. However, in a full 2D simulation, presence of turbulence due to centrifugal barrier is expected to shift the shock farther out. As the incoming matter hits the centrifugal barrier, some matter bounce back and interact with the incoming matter. Thus a turbulence is generated. This turbulent pressure seems to be comparable to the other pressure effects, such as thermal and ram pressure (MLC94, MRC96). This turbulent pressure shifts the location of the shock further out compared to the location which we calculate using one-dimensional analytical method. Interestingly this is precisely what we see.

In Fig. 4, we present the contours of normalized density inside the accretion disc at four different times. Associated colour bar represents the values of the normalized density. Velocity vectors are overplotted with density. The length of a vector is proportional to the magnitude of velocity at that location. The simulation is carried out till the time of 30 000 and we measure the dynamical time to be $t_{\rm dyn} \sim 1500$. Thus, the simulation continued for at least 20 dynamical times without any significant time evolution and hence, we believe that the system has reached a steady state.

Fig. 4(a) shows the density and velocity vectors at time 158 ($t_{\rm dyn} \sim 0.11$), a little after the simulation started. Fig. 4(b) shows the same at time 496 ($t_{\rm dyn} \sim 0.33$), soon after matter reaches $r_{\rm in}$. It can be seen that a shock structure already started forming by this time. The shock front can be identified by the jump in density colour contour close to the axis and also a sudden reduction of

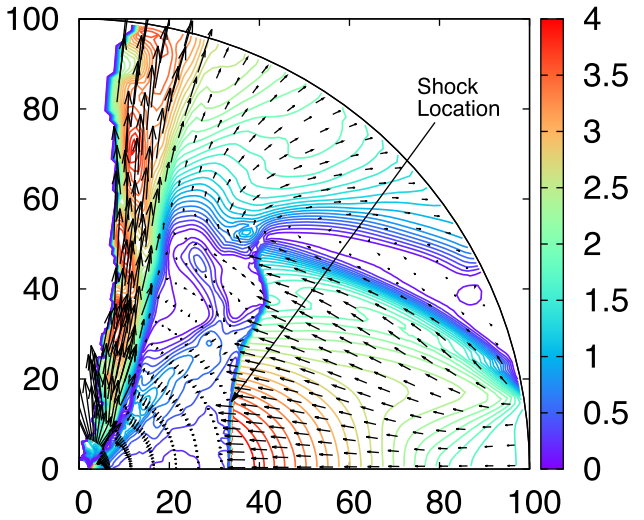

Figure 5. Mach number contours at the final time, overplotted with velocity vectors. It can be seen that the high-velocity outflow leaves the computational domain supersonically.

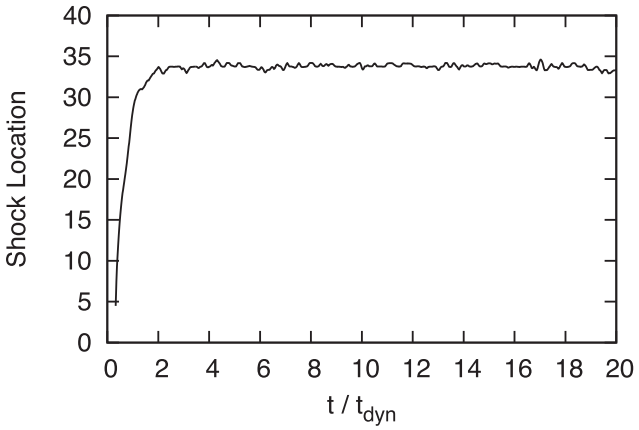

Figure 6. Time variation of shock location. The shock structure is steady, although it oscillates slightly about its mean location of ∼33.8.

velocity vector lengths. The contours clearly look like those of a thick accretion disc as discussed in MLC94 also for a pseudo-Newtonian simulation. As we move up in the vertical direction from the equatorial plane, the shock front bends outwards. This is explained in MRC96; Chakrabarti 1996d as due to the reduction of gravitational pull with height, while the centrifugal force which remains almost the same, pushes the shock outward. This shock front moves away radially from the black hole and stabilizes at a radial distance of ∼33.8. This can be seen in Fig. 4(c) which is a snapshot at nearly 1.5 dynamical times, i.e. 2250. Fig. 4(d) shows the snapshot at a final time of 30 000 ($t_{\rm dyn} \sim 20$). There appears to be practically no change in the shock location or the flow behaviour at this period of the simulation. We ran this simulation at 600 × 200 resolution and found that the results presented here are converged. We also ran this simulation at 150 × 50 resolution by placing $r_{\rm in}$ at 2.5. Even for this lower resolution, the shock location and the overall structure of the disc is found to be very similar to the presented results. Velocity vectors in Figs 4(c) and 4(d) also show that a strong outflow emerges from the post-shock region or CENBOL. In order to prove that it indeed leaves the system supersonically, we plot in Fig. 5 the contours of radial Mach number. As the colour code would indicate, the inward flow became highly supersonic in the pre-shock region and highly subsonic in the post-shock region. It became supersonic again closer to the black hole as it moves to satisfy the boundary condition on the horizon. The outflow behaves exactly the opposite way. It starts subsonically from CENBOL surface and becomes supersonic by the time it reaches at about 10 Schwarzschild radii. The raggedness of the contours on the funnel-like vortex surface close to the axis is due to the artefact of finite-sized grids whose size increases with radial distance from the black hole. In Fig. 6, we present the time evolution of the shock location close to the equatorial plane. We dynamically compute the shock location by picking up the position where the Mach number changes from $M > 1$ to $M < 1$. We have omitted the initial transient time from this plot when the floor grids were being filled by the incoming flow for the first time. Fig. 6 shows that the shock location has achieved a steady state, although it oscillates slightly about its mean location of $r \sim 33.8$, possibly due to the finite grid size at this distance.

5 CONCLUSIONS

It has been demonstrated that TCAF model explains spectral and temporal properties of the black hole accretion discs very well. The CENBOL region, which is primarily responsible for emission of hard photons and the outflows, relies on the formation of shock in the sub-Keplerian component in this model. However, the formation of CENBOL was taken for granted only using simulations carried out in pseudo-Newtonian geometry although its genesis lies in properties of an advective flow in the strong gravity limit. In this paper, we performed numerical simulations in fully GR framework in Schwarzschild space–time to see whether a steady shock formation is still possible or not. We presented results of one-dimensional and two-dimensional simulations. For one-dimensional simulations, we tested the code by comparing our results with the steady-state results obtained using analytical methods. We ran our code for sufficiently long time (over 20 dynamical times) the steady state was found to be achieved. Comparisons of radial Mach number variations were shown for spherically symmetric Bondi accretion flow as well as for axisymmetric accretion flow with and without shock. We found a very good match between the two methods even at moderate resolution and these validated the performance of our simulation code. This gave us confidence to delve into unchartered territory of running the code in two-dimensions, where, strictly speaking, a fully self-consistent theoretical result was missing. Here again, we found steady shock formation and the post-shock region can be easily identified to be the CENBOL region used by CT95. We found that a centrifugal force–driven supersonic jet is formed from the surface of the CENBOL. We also plotted the time variation of the shock location close to the equatorial plane. We found that the location slightly oscillates about a mean value of ∼33.8, but overall structure is steady.

The results presented here were obtained from purely hydrodynamical simulations in Schwarzschild space–time. Analytically, it has been shown in C90, C96b that the presence of black hole rotation will affect the structure of an accretion disc. The parameter space of the shock formation is different for prograde and retrograde flows, and locations of the sonic points as well as shock can be closer or away depending on whether the so-called 'spin–orbit' coupling term (arising out of the product of the spin vector of the black hole and the orbital angular momentum vector of the matter) is positive or negative. We will numerically study the effects of black hole rotation on the accretion disc and shock behaviour. Our code would be easily used to study the dragging of

inertial effects also which is expected to affect the outflows and CENBOL behaviour. Furthermore, in the presence of dissipations, such as viscosity and/or heating/cooling, the structure and the location of the CENBOL will change significantly as shown by previous simulations (GGC12, GGC14, GC13, GGC15), performed using pseudo-Newtonian potential. We will explore the effects of these dissipations in future studies using our GR numerical simulation codes and study how the segregation of the flow into two components may happen in GR framework.

ACKNOWLEDGEMENTS

DSB acknowledges support via NSF grants NSF-DMS-1361197, NSF-ACI-1533850, NSF-DMS-1622457. Several simulations were performed on a cluster at UND which is run by the Center for Research Computing. Computer support on NSF's XSEDE and Blue Waters computing resources is also acknowledged.

REFERENCES

Arlt R., Rüdiger G., 2001, A&A, 374, 1035
Arnaud K. A., 1996, in Jacoby G. H., Barnes J., eds, ASP Conf. Ser. Vol. 101, Astronomical Data Analysis Software and Systems V. Astron. Soc. Pac., San Francisco, p. 17
Balbus S. A., Hawley J. F., 1991, ApJ, 376, 214
Banyuls F., Font J. A., Ibáñez J. M., Martí J. M., Miralles J. A., 1997, ApJ, 476, 221
Brandenburg A., Nordlund A., Stein R. F., Torkelsson U., 1995, ApJ, 446, 741
Chakrabarti S. K., 1989, ApJ, 347, 365 (C89)
Chakrabarti S. K., 1990a, Theory of Transonic Astrophysical Flows. World Scientific, Singapore (C90)
Chakrabarti S. K., 1990b, MNRAS, 243, 610
Chakrabarti S. K., 1996a, Phys. Rep., 266, 229
Chakrabarti S. K., 1996b, MNRAS, 283, 325 (C96b)
Chakrabarti S. K., 1996c, ApJ, 464, 664
Chakrabarti S. K., 1996d, ApJ, 471, 237
Chakrabarti S. K., 1997, ApJ, 484, 313
Chakrabarti S. K., Das S., 2001, MNRAS, 327, 808
Chakrabarti S. K., Molteni D., 1993, ApJ, 417, 671 (CM93)
Chakrabarti S. K., Molteni D., 1995, MNRAS, 272, 80
Chakrabarti S. K., Titarchuk L. G., 1995, ApJ, 455, 623 (CT95)
Chakrabarti S. K., Acharyya K., Molteni D., 2004, A&A, 421, 1
Chakrabarti S. K., Mondal S., Debnath D., 2015, MNRAS, 452, 3451
Chatterjee D., Debnath D., Chakrabarti S. K., Mondal S., Jana A., 2016, ApJ, 827, 88
Das S., Chattopadhyay I., Nandi A., Molteni D., 2014, MNRAS, 442, 251
Debnath D., Chakrabarti S. K., Mondal S., 2014, MNRAS, 440, L121
Debnath D., Mondal S., Chakrabarti S. K., 2015a, MNRAS, 447, 1984
Debnath D., Molla A. A., Chakrabarti S.K., Mondal S., 2015b, ApJ, 803, 59
Garain S. K., Ghosh H., Chakrabarti S. K., 2012, ApJ, 758, 114 (GGC12)
Garain S. K., Ghosh H., Chakrabarti S. K., 2013, MNRAS, 437, 1329 (GGC14)
Giri K., Chakrabarti S. K., Samanta M. M., Ryu D., 2010, MNRAS, 403, 516 (GCSR2010)
Giri K., Chakrabarti S. K., 2012, MNRAS, 421, 666
Giri K., Chakrabarti S. K., 2013, MNRAS, 430, 2836 (GC13)
Giri K., Garain S. K., Chakrabarti S. K., 2015, MNRAS, 448, 3221 (GGC15)
Gu W. M., Foglizzo T., 2003, A&A, 409, 1
Gu W. M., Lu J. F., 2006, MNRAS, 365, 647
Harten A., Lax Peter D., van Leer B., 1983, SIAM Rev., 25, 35
Hawley J. F., Balbus S. A., 1992, ApJ, 400, 595
Hawley J. F., Gammie C. F., Balbus S. A., 1995, ApJ, 440, 742
Hawley J. F., Gammie C. F., Balbus S. A., 1996, ApJ, 464, 690
Jana A., Debnath D., Chakrabarti S. K., Mondal S., Molla A. A., 2016, ApJ, 819, 107
Kim J., Kim H. I., Choptuik M. W., Lee H. M., 2012, MNRAS, 424, 830
King A. R., Pringle J. E., Livio M., 2007, MNRAS, 376, 1740
Kotko I., Lasota J.-P., 2012, A&A, 545, 9
Lanzafame G., Molteni D., Chakrabarti S. K., 1998, MNRAS, 299, 799
Lanzafame G., Cassaro P., Schilliró F., Costa V., Belvedere G., Zappalá R. A., 2008, A&A, 482, 473
Lee S. J., Ryu D., Chattopadhyay I., 2011, ApJ, 728, 142
Lee S., Chattopadhyay I., Kumar R., Hyung S., Ryu D., 2016, ApJ, 831, 33
Molteni D., Lanzafame G., Chakrabarti S. K., 1994, ApJ, 425, 161 (MLC94)
Molteni D., Sponholz H., Chakrabarti S. K., 1996a, ApJ, 457, 805
Molteni D., Ryu D., Chakrabarti S. K., 1996b, ApJ, 470, 460 (MRC96)
Molteni D., Tóth G., Kuznetsov O. A., 1999, ApJ, 516, 411
Mondal S., Debnath D., Chakrabarti S. K., 2014, ApJ, 786, 4
Nakayama K., 1992, MNRAS, 259, 259
Nakayama K., 1994, MNRAS, 270, 871
Nobuta K., Hanawa T., 1994, PASJ, 46, 257
Paczyński B., Wiita P. J., 1980, A&A, 88, 23
Shakura N. I., Sunyaev R. A., 1973, A&A, 24, 337
Shibata M., 2003, Phys. Rev. D, 67, 024033
Shu C.-W., Osher S., 1988, J. Comput. Phys., 77, 439
Smak J., 1999, Acta Astron., 49, 391
Toth G., Keppens R., Botchev M. A., 1998, A&A, 332, 1159

This paper has been typeset from a TEX/LATEX file prepared by the author.